Meson screening masses in (2 + 1)-flavor QCD

A. Bazavov,[1] S. Dentinger,[2] H.-T. Ding,[3] P. Hegde,[4] O. Kaczmarek,[2,3] F. Karsch,[2] E. Laermann,[2,*] Anirban Lahiri,[2] Swagato Mukherjee,[5] H. Ohno,[6] P. Petreczky,[5] R. Thakkar,[4] H. Sandmeyer,[2] C. Schmidt,[2] S. Sharma,[7] and P. Steinbrecher[5]

(HotQCD Collaboration)

[1]*Department of Computational Mathematics, Science and Engineering and Department of Physics and Astronomy, Michigan State University, East Lansing, Michigan 48824, USA*
[2]*Fakultät für Physik, Universität Bielefeld, D-33615 Bielefeld, Germany*
[3]*Key Laboratory of Quark & Lepton Physics (Ministry of Education) and Institute of Particle Physics, Central China Normal University, Wuhan 430079, China*
[4]*Center for High Energy Physics, Indian Institute of Science, Bangalore 560012, India*
[5]*Physics Department, Brookhaven National Laboratory, Upton, New York 11973, USA*
[6]*Center for Computational Sciences, University of Tsukuba, Tsukuba, Ibaraki 305-8577, Japan*
[7]*Department of Theoretical Physics, The Institute of Mathematical Sciences, Chennai 600113, India*

(Received 16 September 2019; published 26 November 2019)

We present lattice QCD results for mesonic screening masses in the temperature range 140 MeV $\lesssim T \lesssim$ 2500 MeV. Our calculations were carried out using $(2+1)$ flavors of the highly improved staggered quark action, with a physical value for the strange quark mass and two values of the light quark mass corresponding to pion masses of 160 and 140 MeV. Continuum-extrapolated results were obtained using calculations with a variety of lattice spacings corresponding to temporal lattice extents $N_\tau = 6$–16. We discuss the implications of these results for the effective restoration of various symmetries in the high temperature phase of QCD, as well as the approach toward the perturbative limit.

DOI: 10.1103/PhysRevD.100.094510

I. INTRODUCTION

At high temperatures the properties of strong-interaction matter change from being controlled by hadronic degrees of freedom to deconfined quarks and gluons. While the thermodynamics in the low temperature phase of QCD resembles many features of a hadron resonance gas, with hadrons keeping their vacuum masses, this quickly changes at temperatures close to and above the crossover transition to the high temperature phase. In fact, the zero temperature hadronic degrees of freedom seem to provide a quite satisfactory description of thermal conditions close to the transition to the high temperature phase [1], although there is evidence of thermal modification of the spectrum [2]. At high temperature, however, quarks and gluons deconfine, which also is reflected in properties of hadron correlation functions and the thermal masses extracted from them (see, e.g., [3]). Resonance peaks in spectral functions, which enter the integral representations of thermal hadron correlation functions, broaden and shift with temperature [4]. In spatial correlation functions [5] the finite temporal extents, $0 \le \tau \le 1/T$, of the Euclidean lattice act on spatial quark and antiquark propagators like a finite volume effect, which influences the long-distance behavior of these correlation functions. Their exponential decay at large distances defines screening masses, which differ substantially from the pole masses at zero temperature, and approach multiples of πT at high temperature, which is characteristic of the propagation of free quark quasiparticles in a thermal medium.

The chiral crossover separating the low and high temperature regimes for nonvanishing quark masses is characterized by a smooth but rapid change of the chiral condensate around T_{pc}. The pseudocritical temperature T_{pc}, for the physical value of the ratio of light and strange quark masses, has recently been determined from fluctuations of various chiral observables, $T_{pc} = (156.5 \pm 1.5)$ MeV [6].

Despite a small explicit breaking of the chiral symmetry by the residual light quark masses, the chiral symmetry,

[*]Deceased.

which is spontaneously broken in the hadronic phase, gets effectively restored above T_{pc}. The deconfinement of the light quark and gluon degrees of freedom is believed to be strongly related to the drop of the chiral condensate and the resultant effective restoration of the chiral symmetry. If chiral symmetry is restored then the excitations of the plasma are also expected to carry that information in spatial hadron correlators. In fact, the analysis of spatial hadron correlation functions and their asymptotic large distance behavior [5] is found to be a sensitive tool for studies of different patterns of chiral symmetry restoration at high temperature. Generally it is found in calculations at physical values of the quark masses that the temperature dependence of screening masses differs significantly in quantum number channels sensitive to the restoration of the $SU_L(2) \times SU_R(2)$ chiral flavor symmetry and the anomalous axial $U_A(1)$ symmetry, respectively. While the former will be restored completely at chiral transition temperature in the chiral limit, the latter remains broken also at high temperature by the Adler-Bell-Jackiw anomaly [7–9]. However, with the thermal suppression of nonperturbative breaking effects, which at zero temperature arise, for instance, from the presence of topologically nontrivial gauge field configurations [10], the anomalous axial symmetry may be "effectively restored." It has been argued that the question whether or not the chiral symmetry and anomalous axial symmetry get effectively restored at the same temperature may have significant qualitative consequences for the structure of the QCD phase diagram in the chiral limit [11].

Calculations with staggered fermions [12,13] show evidence for $U_A(1)$ symmetry breaking also above T_{pc} and provide evidence for the close relation between axial symmetry breaking and the density of near-zero eigenmodes [14]. However, to what extent the flavor singlet anomalous axial $U_A(1)$ symmetry gets effectively restored at the chiral phase transition temperature, $T_c^0 = 132^{+3}_{-6}$ MeV [15], which defines the onset of a true phase transition in the chiral limit, is still an open question [16–19].

Several recent lattice QCD calculations performed in 2 and $(2+1)$-flavor QCD with physical quark mass values utilizing overlap and Möbius domain wall [20–25] as well as Wilson [26] fermions observe an effective restoration of the $U_A(1)$ symmetry at temperatures above the pseudocritical temperature T_{pc}, i.e., at about $(1.2\text{–}1.3)T_{pc}$. This is in accordance with earlier findings in calculations of screening masses with staggered fermions, where effective $U_A(1)$ restoration has been observed through the degeneracy of scalar and pseudoscalar correlation functions and screening masses at temperatures $T \gtrsim 1.3T_{pc}$ [12].

One of the motivations of this study is to also determine the extent to which $U_A(1)$ is effectively restored at the chiral crossover temperature through screening masses for which we have performed continuum extrapolation not yet performed in earlier studies. At the level of screening correlators, $U_A(1)$ restoration leads to a degeneracy between the scalar (S) and pseudoscalar (PS) correlators, while chiral symmetry restoration yields a degeneracy between the vector (V) and axial vector (AV) correlators. We calculate mesonic correlation functions numerically using $(2+1)$-flavor lattice QCD for all the possible flavor combinations including light and strange quarks, namely, light ($\bar{u}d$), light strange ($\bar{u}s$), and strange ($\bar{s}s$). Within each flavor combination, we determine scalar, pseudoscalar, vector, and axial vector ground sate screening masses. The temperature dependence of this set of meson correlation functions has been analyzed before [12], including also charmonia [27], on coarse lattices using the p4 discretization scheme for staggered fermions. With this calculation we substantially improve over earlier work by using the highly improved staggered quark (HISQ) action with physical values for the light and strange quark masses and by performing calculations in a wide range of lattice spacings, $0.017\ \text{fm} \leq a \leq 0.234\ \text{fm}$, that allows us to perform controlled extrapolations to the continuum limit in the temperature range $140\ \text{MeV} \leq T \leq 974\ \text{MeV}$. Albeit not continuum extrapolated, we extend the calculation of screening masses to temperatures as large as 2.5 GeV. Results for screening masses for charmonia, open strange charm, as well as for $\bar{s}s$ channels, with the HISQ action but for only a single lattice spacing corresponding to $N_\tau = 12$, have been reported before [28].

This paper is organized as follows: In the next section, we briefly review properties of spatial meson correlation functions and their evaluation using the staggered fermion discretization scheme. We describe the staggered fermion setup for our calculations in Sec. III. We then present our results in Sec. IV where we start with updating our scale setting in Sec. IV A and present some zero-temperature meson masses. Staggered fermion specific cutoff effects, so-called taste splittings, for $T = 0$ are shown in Sec. IV B. We present results for temperatures around the chiral crossover regime in Sec. IV C where we also discuss effective $U_A(1)$ restoration. In Sec. IV D, we present our results for the screening masses at high temperatures compared to chiral crossover temperature and compare these with predictions from resummed thermal perturbation theory. Finally we state our conclusions in Sec. V. For completeness we have appendixes where we start with an update of the parametrization for scale setting in Appendix A and then in Appendixes B and C, we summarize our statistics in Tables 2–9 and tabulate the continuum-extrapolated values of the screening masses in Tables 10–12 respectively.

II. SPATIAL CORRELATORS AND SCREENING MASSES

Properties of the hadron spectrum at zero and nonzero temperature are commonly determined from an analysis of two-point correlation functions $\langle \mathcal{M}_\Gamma(\mathbf{x})\bar{\mathcal{M}}_\Gamma(\mathbf{y})\rangle$, where the

operators $\mathcal{M}_\Gamma$ project onto a specific set of quantum numbers and $\mathbf{x}$, $\mathbf{y}$ are Euclidean space-time coordinates. At zero temperature the lowest excitation (mass) in a given quantum number channel is conveniently extracted from the asymptotic large Euclidean time behavior of the correlation function. At finite temperature, the calculation of correlators separated in Euclidean time is limited by the limited extent of this direction that determines the inverse temperature of the system, $\beta = 1/T$. In contrast there are no such restrictions for spatially separated correlators, also known as screening correlators.

In QCD, the finite temperature meson screening correlators, projected onto zero transverse momentum ($\mathbf{p}_\perp \equiv (p_x, p_y) = 0$) and lowest Matsubara frequency of a bosonic state ($p_0 \equiv \omega_0 = 0$), are defined by

$$G_\Gamma(z,T) = \int_0^\beta d\tau \int dxdy \langle \mathcal{M}_\Gamma(x,y,z,\tau)\overline{\mathcal{M}_\Gamma}(0,0,0,0)\rangle, \tag{1}$$

where $\mathcal{M}_\Gamma \equiv \bar{\psi}\Gamma\psi$ is a meson operator that projects onto a quantum number channel Γ selected by $\Gamma = \Gamma_D \otimes t^a$ with Dirac matrices Γ_D and a flavor matrix t^a. The angular brackets $\langle\cdots\rangle$, denote the expectation value over the gauge field ensemble. The correlators decay exponentially for large z,

$$G_\Gamma(z,T) \underset{z\to\infty}{\sim} \mathrm{e}^{-m_\Gamma(T)z}, \tag{2}$$

which defines the corresponding screening mass $m_\Gamma(T)$. As already mentioned, for $T \to 0$, the screening masses tend to the mass of the $T = 0$ meson with the same quantum numbers. For $T \to \infty$, they approach the common value $m_\Gamma = 2\pi T$ irrespective of the spin and flavor [5], which indicates that the dominant excitations consist of two almost free fermionic excitations (quarks), which each have a lowest Matsubara frequency (energy) $\omega_0 = \pi T$. For nonzero T, the relation between screening mass and pole mass could be highly nontrivial due to the emergence of nonanalytic structures in the spectral function [29].

On the lattice, the continuum Dirac action must be replaced by a suitable discrete variant. Staggered fermions, which we use in this work, are described by one-component spinors rather than the usual four-component spinors. Because of this, they are relatively inexpensive to simulate. However the price to be paid is that the relation to the continuum theory is subtle. The continuum limit of the theory is the Dirac theory of four fermions rather than one. As a result, each meson too comes in sixteen degenerate copies, which are known as tastes, and the corresponding operators are of the form $\bar{\psi}(\mathbf{x})(\Gamma_D \otimes \Gamma_T^*)\psi(\mathbf{x})$, where $\psi(\mathbf{x})$ is the 16-component hypercubic spinor and Γ_D and Γ_T are Dirac matrices in spin and taste space, respectively. Although different tastes are degenerate in the continuum, on the lattice this degeneracy is broken by gluonic interactions. The masses of the taste partners can be determined from the decay of correlation functions of staggered meson operators $\mathcal{M}(\mathbf{x}) = \sum_{\mathbf{n},\mathbf{n}'} \phi(\mathbf{n},\mathbf{n}')\bar{\chi}(\mathbf{x}+\mathbf{n})\chi(\mathbf{x}+\mathbf{n}')$, where $\mathbf{x}$ is the hypercube coordinate and $\mathbf{n}$ and $\mathbf{n}'$ point to the various vertices of the unit hypercube and ϕ is a site-dependent phase factor whose form depends on the spin and taste quantum numbers of the meson [30–32].

TABLE I. The list of local meson operators studied in this work. States associated with the nonoscillating and the oscillating part of the screening correlators are designated by the identifiers NO and O, respectively. Particle assignments of the corresponding states are given only for the $\bar{u}d$ flavor combination. The superscripts $\mathcal{T}$ and $\mathcal{L}$ stand for transverse and longitudinal, respectively. The operators listed here are the same as in Ref. [12].

		Γ_D		J^{PC}		States	
	$\phi(\mathbf{x})$	NO	O	NO	O	NO	O
$\mathcal{M}1$	$(-1)^{x+y+\tau}$	$\gamma_3\gamma_5$	11	0^{-+}	0^{++}	π_2	a_0
$\mathcal{M}2$	1	γ_5	γ_3	0^{-+}	0^{+-}	π	–
$\mathcal{M}3$	$(-1)^{y+\tau}$	$\gamma_1\gamma_3$	$\gamma_1\gamma_5$	1^{--}	1^{++}	$\rho_2^\mathcal{T}$	$a_1^\mathcal{T}$
$\mathcal{M}4$	$(-1)^{x+\tau}$	$\gamma_2\gamma_3$	$\gamma_2\gamma_5$	1^{--}	1^{++}	$\rho_2^\mathcal{T}$	$a_1^\mathcal{T}$
$\mathcal{M}5$	$(-1)^{x+y}$	$\gamma_4\gamma_3$	$\gamma_4\gamma_5$	1^{--}	1^{++}	$\rho_2^\mathcal{L}$	$a_1^\mathcal{L}$
$\mathcal{M}6$	$(-1)^{x}$	γ_1	$\gamma_2\gamma_4$	1^{--}	1^{+-}	$\rho_1^\mathcal{T}$	$b_1^\mathcal{T}$
$\mathcal{M}7$	$(-1)^{y}$	γ_2	$\gamma_1\gamma_4$	1^{--}	1^{+-}	$\rho_1^\mathcal{T}$	$b_1^\mathcal{T}$
$\mathcal{M}8$	$(-1)^{\tau}$	γ_4	$\gamma_1\gamma_2$	1^{--}	1^{+-}	$\rho_1^\mathcal{L}$	$b_1^\mathcal{L}$

In this work, we only consider *local* operators, i.e., operators with $\mathbf{n} = \mathbf{n}'$. In Table I we list the eight local staggered meson operators that were studied in this work and their mapping to the familiar mesons of QCD. We note that the operators $\mathcal{M}3$, $\mathcal{M}4$, and $\mathcal{M}5$ (respectively, $\mathcal{M}6$, $\mathcal{M}7$, and $\mathcal{M}8$) refer to the x, y, and τ components of the same axial vector (respectively, vector) meson. In the spatial correlation functions the meson operators were separated along the z direction. One thus may average over the $\mathcal{M}3$ and $\mathcal{M}4$ (respectively, $\mathcal{M}6$ and $\mathcal{M}7$) components in order to improve the signal. Note however, that unlike at $T = 0$, at finite temperature one cannot average over all three transverse directions due to the absence of Lorentz invariance in the definition of the correlators [33]. In the vector and axial vector channels we thus deal with two distinct correlation functions and resulting screening masses, denoted as transverse and longitudinal.

A typical staggered meson correlator, for a fixed separation (in lattice unit) between source and sink, is an oscillating correlator that simultaneously couples to two sets of mesons with the same spin but with opposite parities,

$$G_\phi(n_\sigma) = \sum_i \left[A_i^{(-)} \cosh\left(am_{\phi,i}^{(-)}\left(n_\sigma - \frac{N_\sigma}{2}\right)\right) - (-1)^{n_\sigma} A_i^{(+)} \cosh\left(am_{\phi,i}^{(+)}\left(n_\sigma - \frac{N_\sigma}{2}\right)\right)\right], \tag{3}$$

where $n_\sigma = z/a$ denotes the spatial separation of the source and sink operators $\mathcal{M}_\phi$. For large enough distances the correlator of Eq. (3) may be constrained to a single term, i.e., $i = 0$. In Eq. (3) we also replaced the large distance exponential falloff given in Eq. (2) by a hyperbolic cosine that arises due to the periodic nature of correlators on lattices with finite spatial extent N_σ.

III. CALCULATIONAL SETUP

A. Data sets

We calculated the six distinct mesonic correlators, constructed from local staggered fermion operators introduced in the previous subsection, numerically using $(2+1)$-flavor gauge field ensembles generated with the HISQ action and a Symanzik improved gauge action. The HISQ action [34–36] is known to have the least amount of taste splitting [37], due to which it has been used in several precision studies both at $T = 0$ as well as at finite temperature [35,37–40]. The gauge ensembles for $\beta \leq 7.825$ have been generated by the HotQCD collaboration and previously had been used to study the QCD equation of state of strongly interacting matter [41,42]. For $\beta > 7.825$, we have used the gauge ensembles from TUMQCD collaboration, generated for the study of the expectation values of the Polyakov loop and its correlators [43,44]. Gauge configurations have been generated on lattices of size $N_\sigma^3 \times N_\tau$, where $N_\tau = 6$, 8, 10, 12, and 16, and $N_\sigma = 4N_\tau$. Most of the data for these five different values of the temporal lattice size, corresponding to five different values of the lattice spacing a at fixed value of the temperature $T = 1/(N_\tau a)$, have been collected in a temperature range 140 MeV $\leq T \leq$ 172 MeV using physical values of the light (m_l) and strange (m_s) quark masses, i.e., a quark mass ratio $1/27$. On lattices with temporal extent $N_\tau = 8, 10$, and 12 we also used data sets obtained with a slightly larger quark mass ratio, $1/20$. These data sets cover a larger temperature range up to about 2.5 GeV. The Goldstone pion masses for these two quark mass ratios are 140 MeV for $m_l/m_s = 1/27$ and 160 MeV for $m_l/m_s = 1/20$.

All the above-mentioned gauge configurations used in this analysis have been generated with a strange quark mass tuned to its physical value by tuning the mass of the $\eta_{\bar{s}s}$ meson, $M_{\eta_{\bar{s}s}} = 686$ MeV. This value is based on leading order chiral perturbation theory relation, $M_{\eta_{\bar{s}s}} = \sqrt{2m_K^2 - m_\pi^2}$, between the $\eta_{\bar{s}s}$, π, and K masses. Once the strange quark mass was determined, the light quark mass was set to either $m_l = m_s/27$ or $m_l = m_s/20$, as already discussed. The former choice of quark mass was used for temperatures below and near the chiral crossover temperature, T_{pc}, while the higher quark mass was used at higher temperatures ($T \gtrsim 172$ MeV) where quark mass effects are negligible. The tuning of the strange quark mass, which leads to our line of constant physics, is also discussed in detail in Ref. [41]. All our simulation parameters and the number of gauge field configurations analyzed are summarized in Appendix B.

The conversion of hadron masses, calculated in lattice units, into physical units as well as the determination of our temperature scale requires the calculation of one physical observable that is used for the scale setting. For this purpose we use the kaon decay constant, $f_K = 156.1/\sqrt{2}$ MeV, also used in other thermodynamics studies with the HISQ action. We give the updated parametrizations of $f_K a(\beta)$ in Appendix A.

The purpose of the new calibration of the parametrization of $f_K a(\beta)$ in Appendix A is to improve on the scale at the larger β values in this study. Note that when compared to the previous scale [40,41], this leads to a small $\sim$1% decrease of the lattice spacing at the largest β values compared to the previous scale determination [40,41], while the differences are negligible for $\beta \lesssim 7.0$.

B. Hadron correlation functions

A general meson correlator $\langle \mathcal{M}(\mathbf{x})\bar{\mathcal{M}}(\mathbf{y})\rangle$ consists of quark line connected and disconnected parts. In this work we only focus on flavor nonsinglet mesonic correlators that do not have disconnected contribution. The analysis of chiral symmetry restoration, including the $U_A(1)$ restoration, can be performed using flavor nonsinglet correlators alone [21,45]. The (fictitious) $\eta_{\bar{s}s}$ meson, whose mass was used to fix the bare quark masses, also does not receive any contributions from disconnected diagrams [28].

We generally had to retain up to 2 to 3 states in Eq. (3). Such multistate fits present a challenge as a straightforward fit is often highly unstable. For this purpose we developed a routine to guess the initial parameters directly from the data [46] for different terms of the sum in Eq. (3). We also developed [46] a fit parameter estimation routine that works directly on the oscillating correlators. This method relies on the fact that the mass of the oscillating and nonoscillating part, respectively, is usually roughly of similar size and thus assumes their equality in the first step.

(1) At a small fit interval $[n_{\sigma,\min} : n_{\sigma,\max} = N_\sigma/2]$, perform one state fits on all even points of the correlator and we call the resulting fit parameters say $A_{\phi,0}^{\text{even}}$ and $m_{\phi,0}^{\text{even}}$. Repeat the same for the odd points $(A_{\phi,0}^{\text{odd}}, m_{\phi,0}^{\text{odd}})$.

(2) Assuming similar size of the nonoscillating and oscillating mass, the fit parameters for the combined fit may be estimated with $A_{\phi,0}^{-} = (A_{\phi,0}^{\text{even}} + A_{\phi,0}^{\text{odd}})/2$, $A_{\phi,0}^{+} = (A_{\phi,0}^{\text{even}} - A_{\phi,0}^{\text{odd}})/2$, and $m_{\phi,0}^{-} = m_{\phi,0}^{+} = (m_{\phi,0}^{\text{even}} + m_{\phi,0}^{\text{odd}})/2$.

(3) Using the parameters from step 2 as an initial guess, perform a full one state fit with an oscillating and nonoscillating part.

(4) Increase the fit interval. Guess the mass of the next excited state of either the even or the odd part (we used $m_{\phi,1}^{-/+} = 5/4 m_{\phi,0}^{-/+}$). Adjust the corresponding

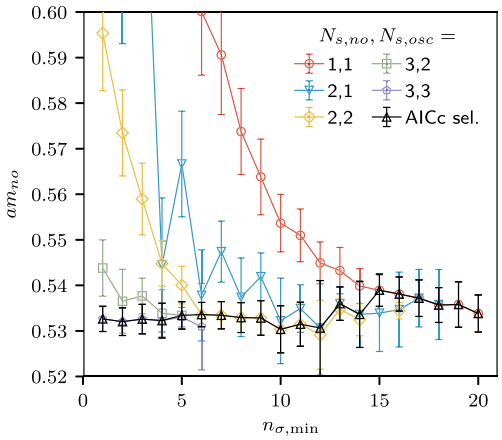

FIG. 1. Screening masses for in the vector channel with a different number of states varying the fit interval for $48^3 \times 12$ lattice for $\beta = 8.710$, which corresponds to $T = 866$ MeV. Fit results selected by the Akaike information criterion (AICc) criterion (shown in black) for different values of minimum distance for the fits seem to fall on a nice plateau.

amplitude ($A^{-}_{\phi,1}$ or $A^{+}_{\phi,1}$) such that the first point of the correlator in the fit interval is reproduced.

(5) Perform a full fit with higher states. Use the parameters from steps 3 and 4 as an initial guess.

(6) Repeat steps 4 to 5 until the desired number of states is reached.

Having developed a method to perform automated multiple state fits, we still have to find which set of fit parameters is the most reasonable one for a given fit interval. For that purpose we have used the corrected AICc [47,48]: For each fit interval we have performed different multiple state fits (maximum three states for oscillating correlators and maximum four states for non-oscillating correlators) and selected the one that has the smallest AICc. In Fig. 1 a comparison between the different multiple state fits and the result that is selected by the AICc is shown. In contrast to the one state fit, this results in an early onset of a stable plateau. After the fits were performed the plateaus were manually selected for each correlator. The final value for the screening mass and its uncertainty are determined by Gaussian bootstrapping. More technical details about the automated fitting procedure can be found in Ref. [46].

We calculated screening correlation functions using point as well as corner wall sources. The point source is the simplest type of source that one can use to calculate mesonic screening functions and we have used one source for each color. However it does not suppress the excited states; therefore, isolating the ground state can be difficult unless the states are well separated or the lattice extent is large. The use of extended (smeared) sources can often help to suppress excited state contributions, allowing to extract the ground state mass and amplitude even on smaller lattices. Here we have used a corner wall source, which

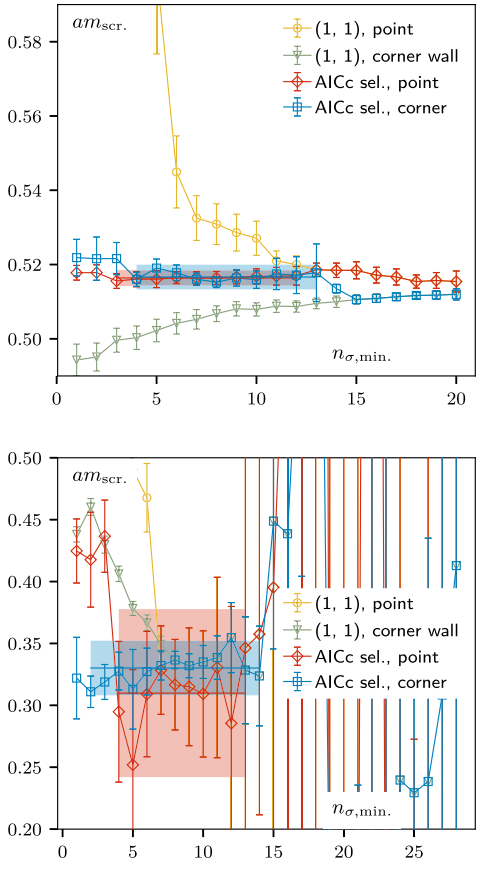

FIG. 2. Comparison of point versus corner wall sources for (top) the scalar ($\mathcal{M}1$) channel using a $48^3 \times 12$ lattice at $T = 769$ MeV and (bottom) the vector (average of $\mathcal{M}6$ and $\mathcal{M}7$) channel using a $64^3 \times 16$ lattice at $T = 146$ MeV. Numbers appearing in parenthesis correspond to the number of states taken in the fit for the nonoscillating and oscillating part of the correlator. The method of using AICc selection criterion to find a plateau among various fits has been described in the main text.

means putting a unit source at the origin of each 2^3 cube on a chosen (in our case) z slice [49–51]. In Fig. 2, we show a comparison of a mass calculation using point and corner wall sources at two different temperatures. As discussed earlier, in both cases we found that it is necessary to take into account contributions from higher excited states to obtain reliable results for the ground state screening masses. In Fig. 2 we have only shown the fit results where we have taken one state for both the oscillating and nonoscillating part of the correlator [denoted by self-explanatory notation (1,1)] and the AICc selected plateaus for the corresponding fit interval. We found that the use of a corner wall source provided advantages only for the noisy correlators, which in particular are the vector and axial vector channels at low temperatures. In the bottom panel of Fig. 2, we provide an example where a corner wall source yielded a better signal as compared to a point source and one gets a longer plateau with smaller

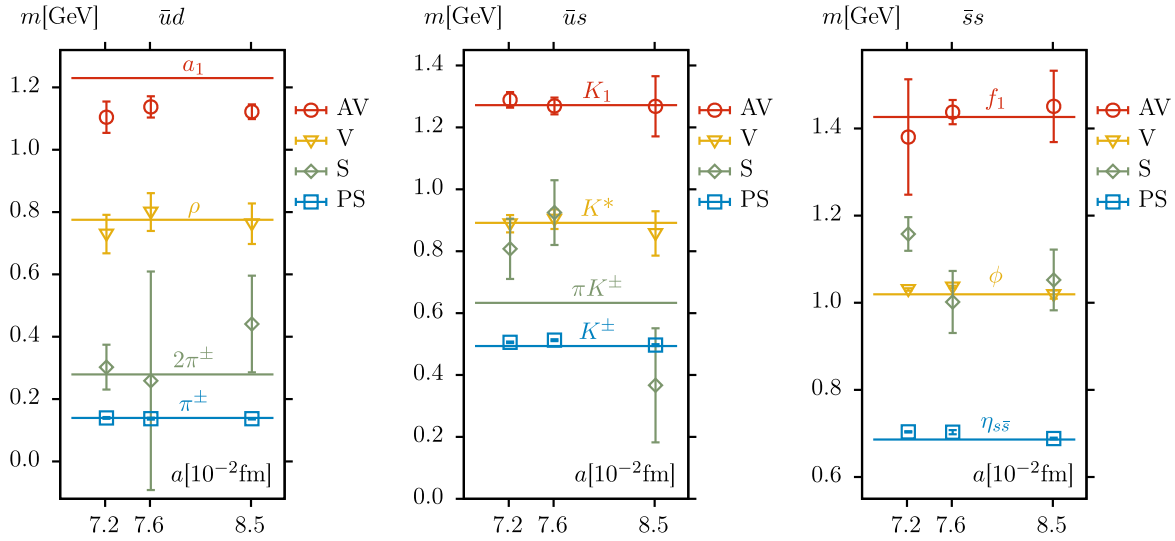

FIG. 3. $T = 0$ masses of the four kinds of mesons studied in this work for the $\bar{u}d$, $\bar{u}s$, and $\bar{s}s$ flavor channels, respectively. Horizontal lines correspond to the physical values of the masses [52]. The scalar meson mass is $2m_\pi$ instead of m_{a0} (or $m_\pi + m_\eta$) due to a staggered artifact at finite lattice spacing. This discrepancy vanishes when the continuum limit of the correlator would be taken before calculating the screening mass [53,54] (see Sec. IV C).

uncertainty when the minimum distance for the fit, $n_{\sigma,\mathrm{min}}$, is varied. Therefore, we used the corner wall source only where it was necessary, i.e., for the vector and axial vector channels below $T = 300$ MeV. For all the other cases however, we found that higher state fits for the point source worked just as well and that their results agreed with the corner wall results. We also found that in the case of a corner wall source, the excited state often has a negative amplitude and, therefore, the influence of the higher states is to shift the result for the screening mass downward rather than upward as can be seen from the top panel of Fig. 2.

IV. RESULTS

A. Scale setting and line of constant physics

As the scale setting calculations as well as the determination of the line of constant physics was performed prior to our current screening mass analysis we tried to reconfirm the scales used in our calculation through additional zero temperature calculations performed on lattices of size 64^4. We performed calculations at three values of the gauge coupling, $\beta = 7.01$, 7.13, and 7.188. Using the parametrization of $f_K a(\beta)$ given in Appendix A this corresponds to lattice spacings $a = 0.085$, 0.076, and 0.072 fm, respectively. The strange quark mass has been fixed using $m_s a(\beta)$ from Ref. [41] and the light quark mass was taken to be $m_l = m_s/27$. The resulting zero temperature meson spectrum is shown in Fig. 3. The solid horizontal lines in the figures correspond to the experimentally determined values of the respective masses [52]. The slight mismatch for $M_{\eta_{\bar{s}s}}$ (m_K), arising from the slight mistuning of the strange quark mass, is visible in the right (middle) panel of Fig. 3. We note that results for most of the PS, V, and AV mesons agree well with the physical zero temperature spectrum within errors. The scalar meson, in the $\bar{u}d$ sector however, seems to have twice the pseudoscalar mass rather than the true scalar mass for the $\bar{u}d$ sector. This is a well-known staggered artifact [53–55] and we also discuss its effect for nonzero temperatures in Sec. IV C. However, such a definite trend is absent in heavier $\bar{u}s$ and $\bar{s}s$ sectors. A slight mismatch can also be observed for the AV masses in the $\bar{u}d$ sector with no definite trend with decreasing lattice spacing.

B. Taste splittings at $T = 0$

Although use of staggered quarks leads to taste splitting in every hadronic channels, its effects are particularly severe in the pseudoscalar sector (π, K, and $\eta_{\bar{s}s}$), since these are the lightest states in the theory. In Fig. 4, we plot the masses of the sixteen different tastes of each of the three pseudoscalar mesons, i.e., π, K, and $\eta_{\bar{s}s}$, for three different values of the lattice spacing. The correlators for the different taste partners are constructed using nonlocal operators [32] with $\Gamma_D = \gamma_5$ and various Γ_T, as shown in Fig. 4. In each case, the lightest meson is the meson with the quantum numbers $\Gamma_T = \Gamma_D = \gamma_5$. This meson is the only Goldstone boson that is massless in the chiral limit at finite lattice spacing and the masses of the other fifteen mesons approach its mass in the continuum limit. The masses of the other partners have been normalized to the mass of the corresponding Goldstone boson for that particular lattice spacing. Our results extend the previous HISQ results for taste splitting to smaller lattice spacings. A more detailed discussion on the taste-splitting effects, also

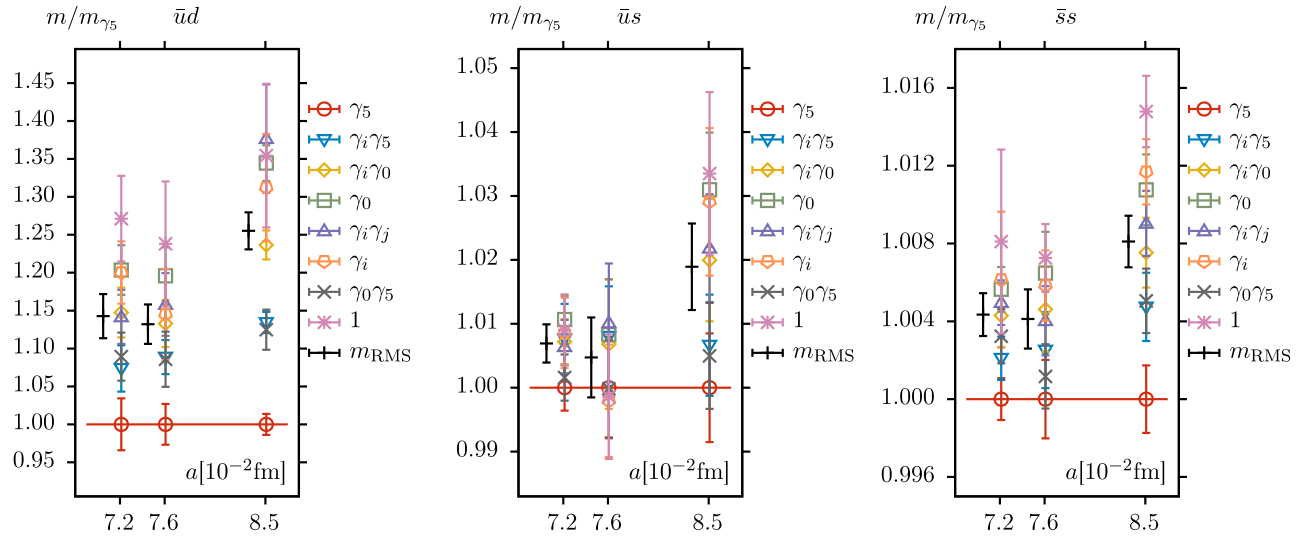

FIG. 4. Masses of the different taste partners of the pseudoscalar mesons, labeled by different Γ_T, for light-light ($\bar{u}d$), light-strange ($\bar{u}s$), and strange-strange ($\bar{s}s$) sectors, normalized to the corresponding Goldstone π, K, and $\eta_{\bar{s}s}$ masses, respectively. The lattice spacings considered here range from approximately 0.085–0.072 fm. Also plotted are the RMS masses defined in Eq. (4).

in comparison to other staggered discretization schemes, can be found in [38,40].

One can define the root mean square (RMS) pion mass m^{PS}_{RMS} as a measure of the taste splitting [56],

$$m^{PS}_{\mathrm{RMS}} = \sqrt{\frac{1}{16}(m^2_{\gamma_5} + m^2_{\gamma_0\gamma_5} + 3m^2_{\gamma_i\gamma_5} + 3m^2_{\gamma_i\gamma_j} + 3m^2_{\gamma_i\gamma_0} + 3m^2_{\gamma_i} + m^2_{\gamma_0} + m^2_{1})}. \tag{4}$$

The γ-matrix suffixes in Eq. (4) refer to the taste structure of the mesons. The RMS mass approaches the Goldstone mass in the continuum limit; hence its deviation from the Goldstone mass at a given lattice spacing is a way of quantifying the taste-breaking effects. The sixteen tastes group into different multiplets, in a way understood from staggered chiral perturbation theory [56]. This is the reason for the factors of 3 in Eq. (4). We find that the RMS taste splitting is of the order of 15%–25% for the light-light ($\bar{u}d$) sector but decreases to about 4%–8% for the strange-strange ($\bar{s}s$) sector. We also see that this splitting decreases as the lattice spacing decreases, as expected. Lastly we note that the masses plotted here are consistent with the trend observed in Fig. 2 of Ref. [40] where the taste splitting was calculated, with the same action but for coarser lattices and a slightly heavier quark mass.

C. Screening masses around the crossover region

We now present our results for screening masses calculated in a range of temperatures going from just below the chiral crossover temperature, $T_{pc} = 156.5(1.5)$ MeV, to about $2T_{pc}$, namely, 140 MeV $\leq T \leq$ 300 MeV. This temperature range is important both from the phenomenological point of view as well as regarding the restoration of chiral $SU_A(2)$ and axial $U_A(1)$ symmetries. As already mentioned earlier, our screening masses were calculated at two values of the light quark mass, viz. $m_l = m_s/27$ for $T \lesssim 172$ MeV and $m_l = m_s/20$ for all higher temperatures. It is worth mentioning here that we have also calculated screening masses with $m_l = m_s/20$ for $T \lesssim 172$ MeV but we do not show them here because we have fewer statistics compared to that for $m_l = m_s/27$. For higher temperatures, the quark mass dependence is negligible and the heavier quark mass can be used without affecting any of the conclusions.

Using the fitting procedure described in Sec. III, we calculated screening masses for five different values of the lattice spacings corresponding to $N_\tau = 6$, 8, 10, 12, and 16, which allow for a continuum extrapolation. As the temperatures do not agree among the different lattices, the screening masses have to be interpolated between the different temperature values. In our extrapolation method, the interpolation and the extrapolation are performed in one single fit: For the interpolation we use simple splines. Then, the extrapolation is performed by replacing the spline coefficients by a function linear in $1/N^2_\tau$ and performing a joint fit that includes all the data. The spline's knot positions are placed according to the density of data points. The knots are positioned in such a way that the same number of data points lies between each pair of subsequent knots. This means, in particular, that more knots are used at

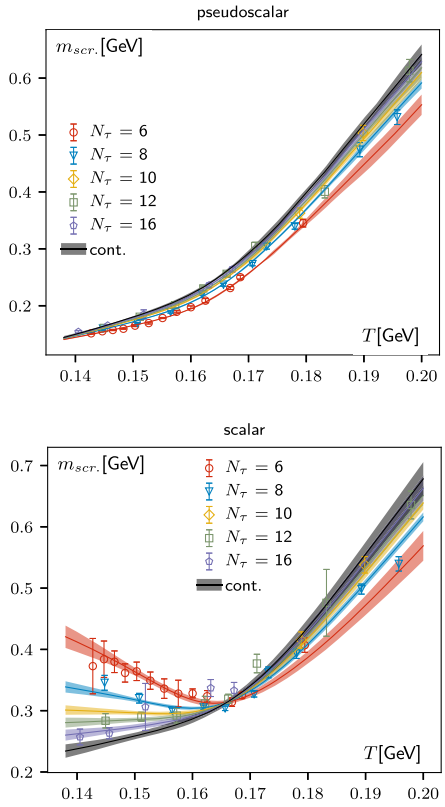

FIG. 5. Examples for the continuum extrapolations for the pseudoscalar (top), scalar (bottom) screening masses in a reduced temperature range. The data for different N_τ were fitted to an N_τ-dependent fit function. Also shown in each figure are the bands for each N_τ, obtained using the same fit function.

the low temperature region, where the interpolation is more curvy. To stabilize the spline, we use some of its coefficients, to constrain the spline's derivative with respect to T at some points. These constraints are placed far outside of the actual region where the extrapolation is performed [46]. The error bands are computed using Gaussian bootstrapping and by performing the extrapolation on each sample. Final values and errors are calculated using median and 68% percentiles of the bootstrap distribution. In Fig. 5 we show two examples of continuum extrapolations following the above-mentioned procedure in the PS and S sector for a limited temperature range. More technical details of the continuum extrapolations can be found in Ref. [46]. Continuum extrapolated masses of all four channels for all three flavor combinations have been tabulated in Appendix. C.

We plot the screening masses for $140\ \text{MeV} \leq T \leq 300\ \text{MeV}$, for the different flavor sectors and for all lattice spacings, in Fig. 6. The mesons with angular momentum $J = 0$ (S and PS) were easier to determine, especially for lower temperatures, as compared to the $J = 1$ mesons (V and AV). We find some cutoff dependence in the scalar sector, especially for smaller N_τ. For the other sectors, the cutoff dependence was indistinguishable within the statistical error. We perform the continuum limit for all the sectors, using data from five different values of the cutoff corresponding to our five different values of the temporal lattice extent, mentioned earlier. The resulting continuum extrapolated bands are plotted in Fig. 7. In Figs. 6 and 7 we also show the pseudocritical temperature region as a gray vertical band. The massless infinite temperature limit $m_{\text{scr}}^{\text{free}} = 2\pi T$ is shown as a dashed line in each of the plots.

For $T \ll T_{pc}$ the screening masses are expected to approach the mass of the lightest zero temperature meson with the same quantum numbers; e.g., the $\bar{u}d$ pseudoscalar screening mass should approach the pion mass m_π. We see that this behavior is readily realized for the PS and V sectors. Already for $T \lesssim 0.9 T_{pc}$ the corresponding zero temperature masses are approached in the $\bar{u}d$, $\bar{u}s$, and $\bar{s}s$ sectors to better than 10%. Although the zero temperature limits are not yet reached in the AV channel at this temperature, we see clear indications for a rapid approach to the corresponding zero temperature masses for all combinations of heavy and light quarks. These values are in all cases approached from below, i.e., at the pseudocritical temperature the AV screening masses are

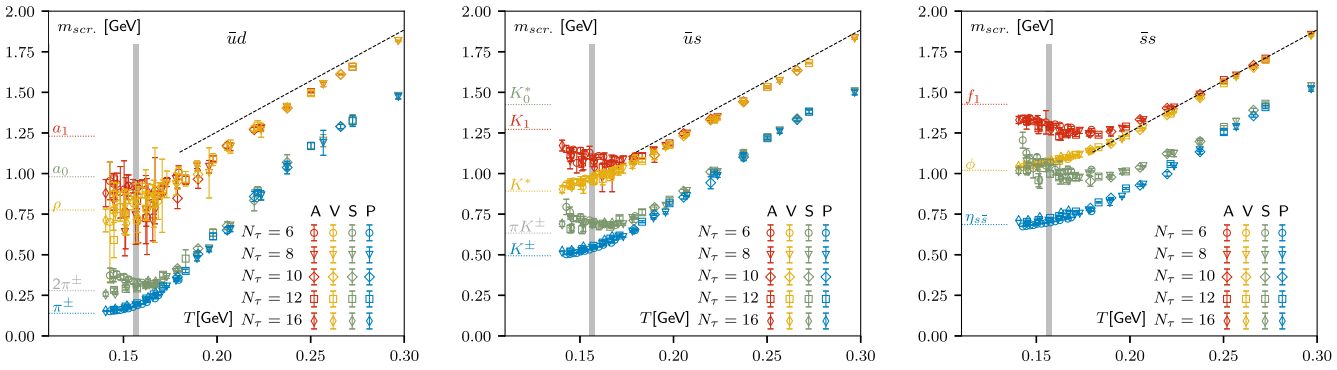

FIG. 6. (Left to right) Results for all four screening masses for the $\bar{u}d$, $\bar{u}s$, and $\bar{s}s$ flavor combinations. The gray vertical band in all the figures represents the pseudocritical temperature, $T_{pc} = 156.5(1.5)$ MeV [6]. The dashed lines corresponds to the free theory limit of $m = 2\pi T$.

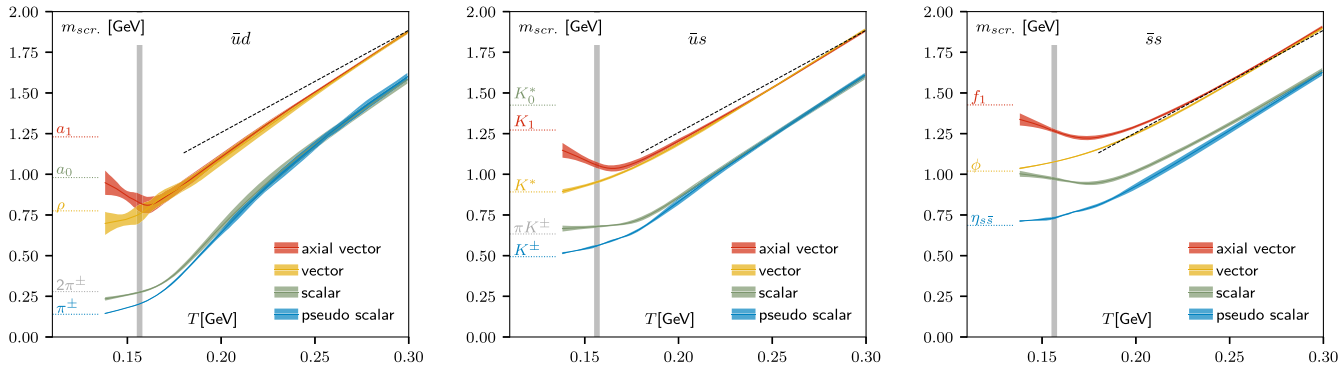

FIG. 7. Continuum bands for screening masses of all four types of mesons for $\bar{u}d$, $\bar{u}s$, and $\bar{s}s$ (left to right).

smaller than the corresponding zero temperature masses. In the $\bar{s}s$ sector the screening mass of the f_1 meson is about 15% lower than the f_1 mass around T_{pc} and reduces to about 7% already at $T \lesssim 0.9T_{pc}$. The situation is similar in the $\bar{u}s$ sector. However, thermal effects are substantially larger in the $\bar{u}d$ sector. Here we find that the screening mass of the a_1 mesons at T_{pc} differs by about 35% from the corresponding zero temperature mass and the two masses still differ by about 20% at $T \lesssim 0.9T_{pc}$. Note that also from our calculations for $m_l = m_s/20$, where we have results at even lower temperatures, we found that the screening masses go towards corresponding zero temperature masses steeply. Similar behavior was also found in calculations with staggered fermions utilizing the p4 discretization scheme [12].

The situation is far more complicated in the S sector for finite lattice spacings. In nature, the lightest flavored scalar meson is either the $a_0(980)$ or the $a_0(1450)$. Rather than either of these values, as can be seen from the left panel of Figs. 6 and 7, the scalar screening mass approaches the value $2m_\pi$ instead. The reason for this is that for staggered fermions, the scalar can decay into two pions at finite lattice spacing [53]. This decay is forbidden in nature due to parity, isospin, and G-parity (I^G) conservation. The unphysical behavior in the staggered discretization comes from the contribution of the different tastes in the intermediate states of loop diagrams. If one takes the continuum limit for the correlator before calculating the screening mass, then the contribution from different tastes cancels out and the physical behavior is recovered [53–55]. Since we, however, calculate the screening masses first and then take the continuum limit, we obtain the unphysical $\pi\pi$ state rather than the true scalar ground state or the physically allowed $\pi\eta$ decay. The unphysical decay only occurs for mesons with isospin $I = 1$. For the $\bar{u}s$ case ($I = 1/2$), the decay to $K\pi$ actually occurs in nature. In Figs. 6 and 7, we see that the scalar screening mass indeed tends to $m_\pi + m_K$ as $T \to 0$.

As the crossover temperature is approached, the vector and axial vector screening masses should become equal due to effective restoration of chiral symmetry. At $T = 0$, the axial vector meson a_1 is about 500 MeV heavier than the vector meson ρ. As the temperature is increased, the AV screening mass decreases while the V mass increases slightly until the two masses become degenerate right at the pseudocritical temperature (left panel of Fig. 7). In contrast, in the $\bar{u}s$ and $\bar{s}s$ sectors, AV and V masses become equal at higher temperatures compared to T_{pc}. Moreover, the relative change of AV masses with respect to V masses from low temperature towards degeneracy temperature progressively decreases when one goes from $\bar{u}d$ to $\bar{s}s$. It must be noted that the approach is nevertheless smoother compared to previous results that were obtained using the p4 discretization scheme for staggered fermions [12]. Crossover temperature, as noted from Fig. 7, is quite similar to what has been seen in the calculation of nucleon masses, where the mass of one particular parity (the one with higher zero temperature mass) of nucleon changes a lot and comes close to its parity partner, which on the contrary hardly changes from low temperature towards chiral crossover temperature [2,57,58].

In Fig. 7, we also see that the scalar and pseudoscalar screening masses in the $\bar{u}d$ sector become degenerate around $T \sim 200$ MeV. Unfortunately, one cannot immediately draw any conclusions about an effective $U_A(1)$ restoration from this due to the pathology of the $\bar{u}d$ scalar correlator that we have discussed above. However, as we have already mentioned, the unphysical contribution cancels out if one would take the continuum limit for the correlator first. Moreover, as the pion screening mass increases around the crossover region while the continuum scalar screening mass is expected to decrease around T_{pc} before rising again at higher temperatures, this unphysical decay channel might be closed around T_{pc} due to lack of phase space. Therefore the degeneracy of the screening masses in the S and PS channel around $T \sim 200$ MeV is an indication towards an effective restoration of the $U_A(1)$.

Despite the above argument, we may nevertheless try and estimate the effective $U_A(1)$ restoration temperature directly from the correlators. Although it is difficult to calculate the continuum limit of staggered correlators due to their oscillating behavior, one may instead consider the corresponding susceptibility, which is given by the integrated

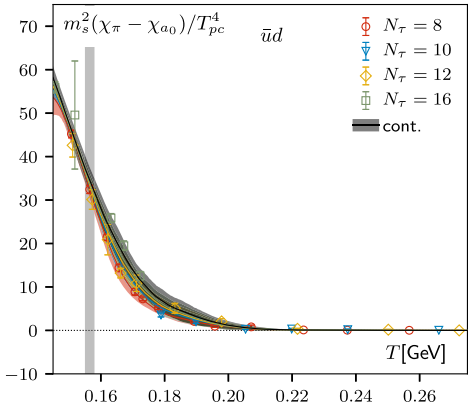

FIG. 8. Difference between the pseudoscalar and scalar susceptibilities as a function of the temperature. The difference is multiplied by m_s^2 to renormalize and normalized to $1/T_{pc}^4$. The continuum extrapolation is also shown in the figure as a superimposed band.

correlator, and calculate its continuum limit instead. The staggered π and δ susceptibilities are defined as

$$\chi_\pi = \sum_{n_\sigma=0}^{N_\sigma-1} G_{\mathcal{M}2}(n_\sigma), \quad \chi_{a_0} = -\sum_{n_\sigma=0}^{N_\sigma-1} (-1)^{n_\sigma} G_{\mathcal{M}1}(n_\sigma). \tag{5}$$

We plot our results, along with the continuum extrapolations, for the difference of the scalar and pseudoscalar susceptibilities for the $\bar{u}d$ sector in Fig. 8. In order to be able to take the continuum limit, we have renormalized the quantity with m_s^2. We have also normalized these numbers to T_{pc}^4. For reference, we also show the pseudocritical temperature region by a gray band in the figure. For the $\bar{u}d$ sector we see that the difference is nonzero around the pseudocritical temperature and only goes to 0 for $T \sim 200$ MeV. There are some theoretical arguments in favor of effective $U_A(1)$ restoration at the chiral phase transition [59] in the chiral limit. On the other hand lattice calculations, performed away from the chiral limit, have found evidence in favor of this scenario [14,20,23,60].

Before moving on, we note that the behavior of the screening masses and susceptibilities in the $\bar{u}s$ and $\bar{s}s$ sectors is qualitatively the same although the degeneracies discussed above occur at progressively higher temperatures [46]. This mass ordering of degeneracy temperatures is in complete accordance with what has been observed for even heavier sectors [28], although one has to keep in mind that the mass effects in the susceptibilities for heavier sectors are expected to be much larger than the $U_A(1)$ breaking effects due to quantum fluctuations.

D. Screening masses at high temperatures

In the previous subsection we have seen that the temperature dependence of the screening masses at $T > 250$ MeV qualitatively follows the free theory expectations; namely, the screening masses are proportional to the temperature, with proportionality constant not very different from 2π. Furthermore, the AV and V screening masses are close to the free theory expectations, while the PS and S screening masses are 10%–20% smaller. In this subsection we study the screening masses at higher temperature with the aim to see how the degeneracy of $PS(S)$ and $AV(V)$ screening masses expected in the infinite temperature limit sets it. We would like to see if contacts to the weak coupling calculations can be made at high temperatures.

Although attempts have been made [5,58,61–66] to compare screening masses from lattice QCD to those from weak coupling calculations, it is not clear in which temperature range weak coupling results can be reliable. For this reason it is important to perform lattice calculations at as high temperatures as possible. Therefore, we extended the calculations of the meson screening masses to $T = 1$ GeV using four lattice spacings corresponding to $N_\tau = 6$, 8, 10, and 12, and performed the continuum extrapolations. The results are shown in Fig. 9. We find that the lattice spacing dependence is very small for $T > 300$ MeV, and within errors the $N_\tau = 8$ results agree with the continuum extrapolated values. Therefore, for 1 GeV $< T <$ 2.5 GeV, we calculated the screening masses using only $N_\tau = 8$ lattices. The results of these calculations are also shown in 9. We clearly see from the figure that the AV and V screening masses overshoot the free theory value around $T = 400$ MeV and are almost constant in temperature units. The PS and S screening masses overshoot the free theory expectation only at temperature larger than 1 GeV and remain smaller than the AV and V screening masses up to the highest temperature considered.

The behavior of the screening masses in the weak coupling picture beyond the free theory limit can be understood in terms of dimensionally reduced effective field theory, called electrostatic QCD (EQCD) [69]. This approach turned out to be useful for understanding the lattice on the quark number susceptibilities [70,71], the expectation value of Polyakov loop [43], and the Polyakov loop correlators [44]. It is interesting to see if deviation of the screening masses at high temperature from $2\pi T$ can be understood within this framework.

In EQCD the correction to the free theory value for the screening masses is obtained by solving the Schrödinger equation in two spatial dimensions with appropriately defined potential [67,72,73]. At leading order the potential is proportional to the coupling constant of EQCD, g_E^2 [67], which in turn can be expressed in terms of the QCD coupling constant $g^2 = 4\pi\alpha_s$. At leading order $g_E^2 = g^2 T$, and g_E^2 has been calculated to two loops [68]. Moreover, at leading order the potential and the correction to the free theory value are independent of the spin; i.e., the $PS(S)$ and $AV(V)$ screening masses receive the same correction that has been calculated in Ref. [67]. This correction is positive in qualitative agreement with our lattice results. In Fig. 9 we

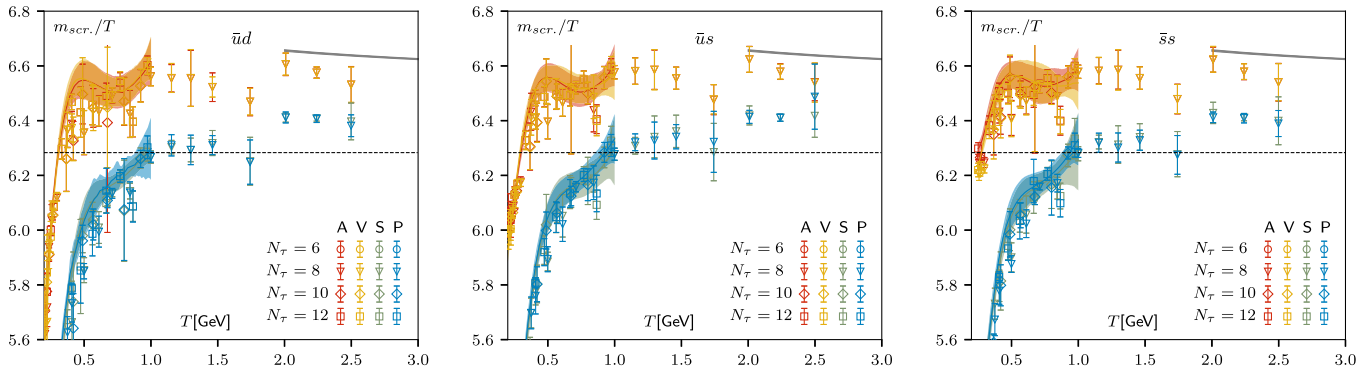

FIG. 9. Screening masses divided by the temperature, for temperatures $T \gtrsim 200$ MeV and for $N_\tau = 6$, 8, 10, and 12 for all four channels in different flavor sectors. The gray curve in the top right part of each figure is the resummed perturbation theory prediction [67,68]. The horizontal dashed line in each plot is the infinite-temperature limit $m_{\mathrm{scr}}^{\mathrm{free}}/T = 2\pi$. Both the infinite-temperature limit as well as the perturbative result are the same for all screening masses irrespective of their spin. Beyond $T \gtrsim 1$ GeV, only $N_\tau = 8$ data exist as a result of which a continuum extrapolation is not possible. The lattice results are obtained with corner wall source for V and AV channels for $T \lesssim 300$ MeV and with point source elsewhere.

show the corresponding weak coupling result from EQCD. We used the two-loop result for g_E^2 and the optimal choice for the renormalization scale $\mu/T = 9.08$ [68]. We varied the scale μ by a factor of 2 around this optimal value to estimate the perturbative uncertainty, which turned out to be very small (the uncertainty corresponds to the width of the weak coupling curve in Fig. 9). We see that the weak coupling results from EQCD are slightly larger than the $AV(V)$ screening masses and significantly larger the lattice results for $PS(S)$ screening masses. This is not completely surprising because the EQCD coupling constant g_E^2 is not small except for very high temperatures and thus higher order corrections may be important. Beyond $\mathcal{O}(g_E^2)$ the correction will be spin dependent [72,73]. Since the coupling constant decreases logarithmically the screening masses approach $2\pi T$ only for temperatures many orders of magnitude larger than those considered here, when the $AV(V)$ and $PS(S)$ screening masses become degenerate. It would be interesting to calculate the $\mathcal{O}(g_E^4)$ correction to meson screening masses and see whether EQCD predictions work quantitatively.

V. CONCLUSIONS

We have performed an in-depth analysis of mesonic screening masses in $(2+1)$-flavor QCD with physical (degenerate) light and strange quark masses. In the vicinity of the pseudocritical temperature for chiral symmetry restoration, T_{pc} and up to about 1 GeV we could perform controlled continuum extrapolations, using input from five different values of the lattice cutoff. Comparing screening masses for chiral partners, related through the chiral $SU_L(2) \times SU_R(2)$ and the axial $U_A(1)$ transformations, respectively, we find in the case of light-light mesons evidence for the degeneracy of screening masses related through the chiral $SU_L(2) \times SU_R(2)$ at or very close to T_{pc} while screening masses related through an axial $U_A(1)$ transformation start becoming degenerate only at about $1.3T_{pc}$. In particular, the V and AV mesons ($J = 1$), which are related by chiral $SU_L(2) \times SU_R(2)$ transformations, become degenerate at $T \simeq T_{pc}$, while the S and the PS ($J = 0$) mesons, which are related by axial $U_A(1)$ transformations, only become degenerate around $1.3T_{pc}$. The onset of these degeneracies also occurs in the light-strange and strange-strange meson sectors, but at higher temperatures.

At high temperatures the screening masses overshoot the free theory expectations in qualitative agreement with the weak coupling calculations at $\mathcal{O}(g_E^2)$. While mesonic screening masses in given angular momentum (J) channels become degenerate, screening masses in channels with different J, e.g., $J = 0$ and $J = 1$, stay well separated even up to the highest temperature, $T = 2.5$ GeV, that was analyzed by us. We argued that it is necessary to go beyond $\mathcal{O}(g_E^2)$ calculations in order to understand this feature within the EQCD framework. This nondegeneracy has also been observed in Ref. [74], where it was also shown that these two sets of mesons only become degenerate at asymptotically high temperatures. This conclusion is in agreement with the results that we have presented in this paper in Sec. IV D (Fig. 9).

ACKNOWLEDGMENTS

This material is based upon work supported by the U.S. Department of Energy, Office of Science, Office of Nuclear Physics in the following ways: (i) Through Contract No. DE-SC0012704, (ii) within the framework of the Beam Energy Scan Theory (BEST) Topical Collaboration, and (iii) through the Scientific Discovery through Advanced Computing (SciDAC) award Computing the Properties of Matter with Leadership Computing Resources.

This research also was funded by the following: (i) the Deutsche Forschungsgemeinschaft (DFG, German Research Foundation) through Grant No. CRC-TR 211 "Strong-interaction matter under extreme conditions"—project number 315477589—TRR 211; (ii) Grant No. 05P18PBCA1 of the German Bundesministerium für Bildung und Forschung; (iii) Grant No. 283286 of the European Union; (iv) the U.S. National Science Foundation under Grant No. PHY-1812332; (v) The Early Career Research Award of the Science and Engineering Research Board of the Government of India; (vi) the Ramanujan Fellowship of the Department of Science and Technology, Government of India; and (vii) the National Natural Science Foundation of China under Grants No. 11775096 and No. 11535012.

This research used awards of computer time provided by the following: (i) the INCITE and ALCC programs Oak Ridge Leadership Computing Facility, a DOE Office of Science User Facility operated under Contract No. DE-AC05-00OR22725; (ii) the ALCC program at National Energy Research Scientific Computing Center, a U.S. Department of Energy Office of Science User Facility operated under Contract No. DE-AC02-05CH11231; (iii) the INCITE program at Argonne Leadership Computing Facility, a U.S. Department of Energy Office of Science User Facility operated under Contract No. DE-AC02-06CH11357; and (iv) the USQCD consortium at its Jefferson Laboratory and Fermilab computing facilities. This research would like to acknowledge the following for computing resources: (i) The GPU supercomputing cluster of Bielefeld University, (ii) PRACE for awarding us access to Piz Daint at CSCS, Switzerland, and Marconi at CINECA, Italy, and (iii) JUWELS at NIC Juelich, Germany.

APPENDIX A: PARAMETRIZATION OF $f_K a(\beta)$ FOR SCALE SETTING

For the scale setting in this project we used the kaon decay constant, i.e., $f_K a(\beta)$. Including the measurements up to $\beta = 7.373$, listed in Ref. [41], we have updated the parametrization used in Ref. [40],

$$f_K a(\beta) = \frac{c_0 f(\beta) + c_2 (10/\beta) f^3(\beta)}{1 + d_2 (10/\beta) f^2(\beta)}, \qquad \text{(A1)}$$

where

$$f(\beta) = \left(\frac{10 b_0}{\beta}\right)^{-b_1/(2b_0^2)} \exp(-\beta/(20 b_0)),$$

with b_0 and b_1 being the coefficients of the two-loop beta function. For the three-flavor case, $b_0 = 9/(16\pi^2)$ and $b_1 = 1/(4\pi^4)$. The updated fit renders the following parameters for the form described in Eq. (A1): $c_0 = 7.49415$, $c_2 = 46049(1248)$, and $d_2 = 3671(137)$. We have not included the $f_K a(\beta)$ measurements for the two highest β values, shown in Fig. 10 because of possible large finite volume effects.

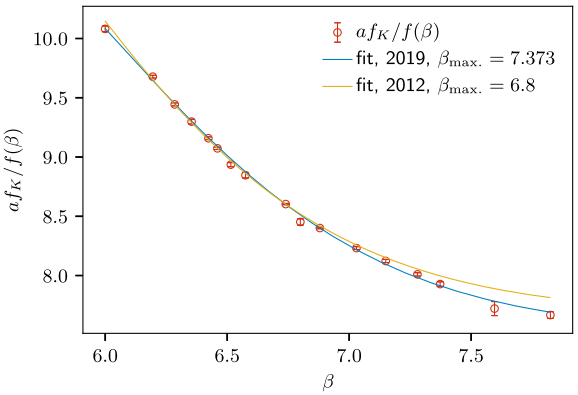

FIG. 10. Comparison of updated $f_K a(\beta)$ parametrization and the older one from Ref. [40].

In Fig. 10 we have compared the fit described with Eq. (A1) to the same from Ref. [40]. It can be seen from the plot that one overestimates $f_K a(\beta)$ with the old parametrization for $\beta \gtrsim 6.9$ by $\sim 1\%$. One can look in Refs. [40,41] for more details on this kind of parametrization.

APPENDIX B: SUMMARY OF STATISTICS FOR $m_l = m_s/20$ AND $m_l = m_s/27$

Here we summarize our data sets and the number of configurations on which point and wall source correlators have been calculated are given in the last two columns of the tables, which are labeled point and wall, respectively.

TABLE II. Summary of statistics for $m_l = m_s/20$, $24^3 \times 6$ lattices.

β	T [MeV]	m_l	m_s	Point	Wall
5.850	119.19	0.00712	0.1424	1166	1166
5.900	125.45	0.00660	0.1320	1000	1000
5.950	132.07	0.00615	0.1230	1000	1000
6.000	139.08	0.00569	0.1138	3073	3073
6.025	142.73	0.00550	0.1100	1000	1000
6.050	146.48	0.00532	0.1064	1000	1000
6.062	148.32	0.005235	0.1047	1000	1000
6.075	150.33	0.00518	0.1036	1000	1000
6.090	152.70	0.00504	0.1008	1001	1001
6.100	154.29	0.00499	0.0998	3363	3363
6.120	157.54	0.004845	0.0969	1001	1001
6.125	158.36	0.00483	0.0966	1003	1003
6.150	162.54	0.00468	0.0936	1000	1000
6.165	165.10	0.00457	0.0914	1000	1000
6.185	168.58	0.004455	0.0891	1000	1000
6.195	170.35	0.00440	0.0880	1000	1000
6.245	179.46	0.00415	0.0830	1000	1000

TABLE III. Summary of statistics for $m_l = m_s/20$, $32^3 \times 8$ lattices.

β	T [MeV]	m_l	m_s	Point	Wall
6.050	109.86	0.00532	0.1064	2108	2108
6.125	118.77	0.00483	0.0966	2241	2241
6.195	127.76	0.00440	0.0880	1690	1690
6.245	134.60	0.00415	0.0830	2710	2710
6.285	140.32	0.00395	0.0790	2000	2000
6.341	148.74	0.00370	0.0740	1713	1713
6.354	150.76	0.00364	0.0728	1249	1249
6.390	156.50	0.00347	0.0694	2604	2604
6.423	161.93	0.00335	0.0670	2031	2031
6.460	168.24	0.00320	0.0640	1644	1644
6.488	173.16	0.00310	0.0620	1790	1790
6.515	178.03	0.00302	0.0604	3067	3067
6.575	189.29	0.00282	0.0564	3206	3206
6.608	195.75	0.00271	0.0542	2379	2379
6.664	207.17	0.00257	0.0514	2001	2001
6.740	223.58	0.00238	0.0476	831	831
6.800	237.32	0.00224	0.0448	500	500
6.880	256.75	0.00206	0.0412	500	500
7.030	296.81	0.00178	0.0356	500	500
7.280	375.26	0.00142	0.0284	500	500
7.373	408.63	0.00125	0.0250	500	500
7.596	499.30	0.00101	0.0202	500	500
7.825	610.60	0.00082	0.0164	500	500
8.000	710.45	0.00070	0.0140	500	500
8.200	843.20	0.0005835	0.0116	250	250
8.400	999.39	0.0004875	0.00975	250	250
8.570	1153.83	0.0004188	0.008376	200	200
8.710	1298.31	0.0003697	0.007394	200	200
8.850	1460.54	0.0003264	0.006528	200	200
9.060	1742.17	0.0002417	0.004834	200	0
9.230	2009.14	0.0002074	0.004148	200	200
9.360	2240.48	0.00018455	0.003691	200	200
9.490	2498.41	0.00016425	0.003285	200	200
9.670	2905.28	0.00013990	0.002798	0	200

TABLE IV. Summary of statistics for $m_l = m_s/20$, $40^3 \times 10$ lattices.

β	T [MeV]	m_l	m_s	Point	Wall
6.488	138.53	0.00310	0.0620	9534	9534
6.515	142.42	0.00302	0.0604	2525	2525
6.575	151.43	0.00282	0.0564	2512	2512
6.608	156.60	0.00271	0.0542	2685	2685
6.664	165.73	0.00257	0.0514	1071	1071
6.740	178.86	0.00238	0.0476	1021	1021
6.800	189.85	0.00224	0.0448	800	800
6.880	205.40	0.00206	0.0412	650	650
6.950	219.87	0.00193	0.0386	500	500
7.030	237.45	0.00178	0.0356	600	600
7.150	266.03	0.00160	0.0320	500	500
7.500	366.65	0.00111	0.0222	450	450
7.650	419.00	0.00096	0.0192	250	250
7.825	488.48	0.00082	0.016	250	250
8.000	568.36	0.00070	0.0140	500	500
8.200	674.56	0.0005835	0.0116	551	551
8.400	799.51	0.0004875	0.00975	300	300
8.570	923.07	0.0004188	0.008376	250	250

(Table continued)

TABLE V. Summary of statistics for $m_l = m_s/20$, $48^3 \times 12$ lattices.

β	T [MeV]	m_l	m_s	Point	Wall
6.664	138.11	0.00257	0.0514	372	372
6.700	143.20	0.00248	0.0496	649	649
6.740	149.05	0.00238	0.0476	2214	2214
6.800	158.21	0.00224	0.0448	2008	2008
6.880	171.17	0.00206	0.0412	2001	2001
6.950	183.22	0.00193	0.0386	1300	1300
7.030	197.87	0.00178	0.0356	1000	1000
7.150	221.69	0.00160	0.0320	730	730
7.280	250.18	0.00142	0.0284	800	800
7.373	272.42	0.00125	0.0250	800	800
7.596	332.87	0.00101	0.0202	800	800
7.825	407.06	0.00082	0.0164	900	900
8.000	473.63	0.00070	0.0140	310	310
8.200	562.13	0.0005835	0.0116	500	500
8.400	666.26	0.0004875	0.00975	500	500
8.570	769.22	0.0004188	0.008376	250	250
8.710	865.54	0.0003697	0.007394	250	250
8.850	973.70	0.0003264	0.006528	250	250

TABLE VI. Summary of statistics for $m_l = m_s/27$, $24^3 \times 6$ lattices.

β	T [MeV]	m_l	m_s	Point	Wall
6.025	142.73	0.004074	0.1100	990	990
6.038	144.66	0.004	0.1082	1581	1581
6.050	146.48	0.003941	0.1064	1649	1649
6.062	148.32	0.003878	0.1047	1650	1650
6.075	150.33	0.003837	0.1036	1393	1749
6.090	152.70	0.003733	0.1008	1386	1386
6.105	155.10	0.003659	0.0988	1749	1749
6.120	157.54	0.003589	0.0969	1649	1649
6.135	160.02	0.003519	0.0950	1749	1749
6.150	162.54	0.003467	0.0936	990	990
6.175	166.83	0.003356	0.0906	1472	1472
6.185	168.58	0.0033	0.0891	1475	1550

TABLE VII. Summary of statistics for $m_l = m_s/27$, $32^3 \times 8$ lattices.

β	T [MeV]	m_l	m_s	Point	Wall
6.315	144.77	0.00281	0.0759	1115	1115
6.354	150.76	0.00270	0.0728	3731	3731
6.390	156.50	0.00257	0.0694	3514	3514
6.423	161.93	0.00248	0.0670	3250	3250
6.445	165.66	0.00241	0.0652	1912	2373
6.474	170.68	0.00234	0.0632	1937	2425

TABLE VIII. Summary of statistics for $m_l = m_s/27$, $48^3 \times 12$ lattices.

β	T[MeV]	m_l	m_s	Point	Wall
6.712	144.94	0.00181	0.0490	1955	1955
6.754	151.15	0.00173	0.0468	1484	1484
6.794	157.28	0.00167	0.0450	1407	1407
6.825	162.17	0.00161	0.0436	1946	1946
6.850	166.21	0.00157	0.0424	2081	2081
6.880	171.17	0.00153	0.0412	1960	1960

TABLE IX. Summary of statistics for $m_l = m_s/27$, $64^3 \times 16$ lattices.

β	T [MeV]	m_l	m_s	Point	Wall
6.973	140.50	0.00139	0.0376	4817	2757
7.010	145.59	0.00132	0.0357	5919	6168
7.054	151.84	0.00129	0.0348	123	622
7.095	157.87	0.00124	0.0334	0	308
7.130	163.17	0.00119	0.0322	3697	3697
7.156	167.20	0.00116	0.0314	5774	6107
7.188	172.29	0.00113	0.0306	4451	4324

APPENDIX C: CONTINUUM-EXTRAPOLATED VALUES OF THE SCREENING MASSES

Here we have tabulated the continuum extrapolated screening masses of PS, S, V, and AV channels and in each channel for all three flavor combinations, i.e., $\bar{u}d$, $\bar{u}s$, and $\bar{s}s$.

TABLE X. Continuum-extrapolated values of the light-light screening masses.

T [GeV]	m_{P} [GeV]	m_{V} [GeV]	m_{S} [GeV]	m_{A} [GeV]
0.132	0.129(5)	0.7(2)	0.22(2)	1.0(2)
0.136	0.139(4)	0.69(9)	0.23(2)	0.96(9)
0.140	0.150(2)	0.70(7)	0.24(1)	0.94(7)
0.144	0.1615(9)	0.71(5)	0.245(8)	0.91(5)
0.148	0.174(2)	0.72(4)	0.254(6)	0.88(4)
0.152	0.187(2)	0.73(5)	0.263(6)	0.85(4)
0.156	0.202(3)	0.75(6)	0.274(7)	0.83(6)
0.160	0.221(3)	0.78(5)	0.286(7)	0.81(6)
0.164	0.245(2)	0.82(4)	0.303(6)	0.82(5)
0.168	0.275(4)	0.85(5)	0.326(6)	0.84(4)
0.172	0.310(7)	0.88(4)	0.356(9)	0.87(4)
0.176	0.352(8)	0.90(4)	0.39(2)	0.90(4)
0.180	0.399(7)	0.93(4)	0.44(2)	0.94(4)
0.184	0.445(9)	0.96(4)	0.48(2)	0.97(3)
0.188	0.50(1)	0.99(4)	0.53(2)	1.00(3)
0.192	0.54(1)	1.02(4)	0.58(3)	1.04(3)
0.196	0.59(2)	1.05(4)	0.63(3)	1.07(3)
0.200	0.64(2)	1.09(4)	0.68(3)	1.11(3)
0.240	1.08(4)	1.41(2)	1.10(4)	1.43(1)
0.280	1.45(3)	1.73(1)	1.43(3)	1.729(8)
0.320	1.76(2)	2.03(2)	1.74(3)	2.03(2)
0.360	2.06(2)	2.32(2)	2.04(2)	2.32(2)
0.400	2.34(3)	2.61(3)	2.33(2)	2.60(2)
0.440	2.61(3)	2.88(3)	2.61(3)	2.87(3)
0.480	2.88(3)	3.15(4)	2.89(4)	3.14(4)
0.520	3.15(4)	3.41(4)	3.16(4)	3.40(4)
0.560	3.42(5)	3.66(5)	3.42(4)	3.66(5)
0.600	3.68(4)	3.92(5)	3.68(4)	3.92(5)
0.640	3.94(4)	4.17(4)	3.93(3)	4.17(5)
0.680	4.19(4)	4.43(4)	4.19(3)	4.43(5)
0.720	4.45(4)	4.68(4)	4.44(3)	4.68(5)
0.760	4.71(4)	4.94(4)	4.70(3)	4.94(5)
0.800	4.97(4)	5.21(5)	4.96(3)	5.21(5)
0.840	5.23(4)	5.48(5)	5.22(4)	5.48(6)
0.880	5.49(4)	5.76(5)	5.49(3)	5.75(5)
0.920	5.76(6)	6.04(5)	5.75(4)	6.03(6)
0.960	6.02(9)	6.33(6)	6.03(4)	6.32(6)
1.000	6.3(2)	6.63(9)	6.30(5)	6.62(9)

TABLE XI. Continuum-extrapolated values of the strange-light screening masses.

T [GeV]	m_{P} [GeV]	m_{V} [GeV]	m_{S} [GeV]	m_{A} [GeV]
0.132	0.50(2)	0.88(2)	0.66(3)	1.17(6)
0.136	0.51(1)	0.89(2)	0.67(3)	1.16(6)
0.140	0.519(5)	0.90(2)	0.67(2)	1.14(5)
0.144	0.527(2)	0.91(2)	0.67(2)	1.12(3)
0.148	0.537(4)	0.923(9)	0.67(2)	1.10(3)
0.152	0.547(9)	0.936(9)	0.675(9)	1.08(2)
0.156	0.559(7)	0.950(9)	0.679(8)	1.06(2)
0.160	0.574(4)	0.965(9)	0.682(7)	1.04(2)
0.164	0.590(7)	0.982(9)	0.686(5)	1.04(2)
0.168	0.604(4)	1.00(1)	0.690(6)	1.04(2)
0.172	0.621(6)	1.020(9)	0.698(8)	1.05(2)
0.176	0.642(9)	1.041(9)	0.71(2)	1.07(2)
0.180	0.667(9)	1.063(9)	0.73(2)	1.09(2)
0.184	0.697(9)	1.086(9)	0.75(2)	1.11(2)
0.188	0.73(2)	1.11(1)	0.77(2)	1.13(2)

TABLE XI. *(Continued)*

T [GeV]	m_P [GeV]	m_V [GeV]	m_S [GeV]	m_A [GeV]
0.192	0.76(2)	1.13(1)	0.80(2)	1.15(2)
0.196	0.80(2)	1.16(1)	0.83(2)	1.18(2)
0.200	0.83(3)	1.19(2)	0.86(2)	1.20(2)
0.240	1.16(2)	1.461(8)	1.16(2)	1.463(9)
0.280	1.46(2)	1.748(7)	1.46(2)	1.743(7)
0.320	1.76(2)	2.04(2)	1.75(2)	2.03(2)
0.360	2.05(2)	2.32(2)	2.04(2)	2.32(2)
0.400	2.34(2)	2.60(2)	2.33(2)	2.60(2)
0.440	2.62(2)	2.88(3)	2.61(2)	2.88(3)
0.480	2.89(3)	3.15(3)	2.89(3)	3.15(3)
0.520	3.16(3)	3.41(3)	3.16(4)	3.41(3)
0.560	3.42(4)	3.67(3)	3.42(4)	3.67(4)
0.600	3.68(4)	3.93(4)	3.68(4)	3.92(4)
0.640	3.93(4)	4.18(4)	3.94(4)	4.17(4)
0.680	4.19(4)	4.44(4)	4.19(4)	4.43(4)
0.720	4.45(4)	4.69(4)	4.44(4)	4.68(4)
0.760	4.71(4)	4.95(5)	4.69(5)	4.94(5)
0.800	4.97(4)	5.21(4)	4.95(5)	5.21(5)
0.840	5.23(4)	5.48(4)	5.21(5)	5.48(5)
0.880	5.50(4)	5.75(4)	5.47(5)	5.75(4)
0.920	5.77(5)	6.02(5)	5.74(6)	6.03(5)
0.960	6.05(7)	6.29(7)	6.02(8)	6.31(6)
1.000	6.3(1)	6.6(1)	6.3(2)	6.60(8)

TABLE XII. Continuum-extrapolated values of the strange-strange screening masses.

T [GeV]	m_P [GeV]	m_V [GeV]	m_S [GeV]	m_A [GeV]
0.132	0.71(2)	1.026(7)	1.01(3)	1.36(5)
0.136	0.711(8)	1.032(6)	1.01(2)	1.34(5)
0.140	0.714(4)	1.040(5)	1.00(2)	1.33(4)
0.144	0.717(1)	1.048(4)	0.99(2)	1.32(3)

(Table continued)

TABLE XII. *(Continued)*

T [GeV]	m_P [GeV]	m_V [GeV]	m_S [GeV]	m_A [GeV]
0.148	0.720(6)	1.056(3)	0.99(2)	1.30(2)
0.152	0.724(9)	1.065(3)	0.98(2)	1.29(2)
0.156	0.730(9)	1.075(3)	0.97(1)	1.27(2)
0.160	0.744(6)	1.086(3)	0.965(9)	1.25(2)
0.164	0.758(6)	1.098(3)	0.957(7)	1.24(2)
0.168	0.772(5)	1.110(4)	0.949(7)	1.23(2)
0.172	0.783(8)	1.124(4)	0.944(9)	1.22(2)
0.176	0.796(9)	1.138(5)	0.94(2)	1.22(2)
0.180	0.81(1)	1.154(5)	0.95(2)	1.23(2)
0.184	0.831(9)	1.171(6)	0.96(2)	1.24(2)
0.188	0.85(1)	1.189(6)	0.97(2)	1.25(1)
0.192	0.88(2)	1.208(7)	0.98(2)	1.26(1)
0.196	0.90(2)	1.229(7)	1.00(2)	1.277(9)
0.200	0.93(2)	1.250(7)	1.02(2)	1.294(9)
0.240	1.20(3)	1.492(7)	1.25(2)	1.512(7)
0.280	1.48(2)	1.763(7)	1.50(2)	1.772(7)
0.320	1.78(2)	2.04(2)	1.78(2)	2.05(2)
0.360	2.07(2)	2.32(2)	2.06(2)	2.33(2)
0.400	2.35(2)	2.60(3)	2.34(2)	2.61(3)
0.440	2.63(3)	2.88(3)	2.62(3)	2.88(3)
0.480	2.90(3)	3.15(3)	2.89(3)	3.15(3)
0.520	3.17(4)	3.41(3)	3.16(4)	3.41(3)
0.560	3.43(4)	3.68(4)	3.42(4)	3.67(4)
0.600	3.68(4)	3.93(4)	3.68(4)	3.93(4)
0.640	3.94(4)	4.19(5)	3.93(4)	4.19(5)
0.680	4.19(4)	4.45(6)	4.19(4)	4.44(5)
0.720	4.45(3)	4.71(6)	4.44(4)	4.70(5)
0.760	4.70(3)	4.96(6)	4.70(4)	4.96(5)
0.800	4.96(4)	5.22(5)	4.95(4)	5.22(5)
0.840	5.23(4)	5.48(4)	5.21(4)	5.49(5)
0.880	5.50(4)	5.74(4)	5.48(6)	5.76(4)
0.920	5.77(5)	6.01(5)	5.75(8)	6.03(4)
0.960	6.05(6)	6.27(7)	6.0(2)	6.31(6)
1.000	6.3(1)	6.5(2)	6.3(2)	6.59(9)

[1] A. Andronic, P. Braun-Munzinger, K. Redlich, and J. Stachel, Nature (London) **561**, 321 (2018).
[2] G. Aarts, C. Allton, D. De Boni, and B. Jäger, Phys. Rev. D **99**, 074503 (2019).
[3] F. Karsch and E. Laermann, Thermodynamics and in-medium hadron properties from lattice QCD, in *Quark-Gluon Plasma III*, edited by R. C. Hwa and X.-N. Wang (, Singapore, 2003), Vol. 1.
[4] G. Aarts, C. Allton, D. De Boni, S. Hands, B. Jäger, C. Praki, and J.-I. Skullerud, J. High Energy Phys. 06 (2017) 034.
[5] C. E. Detar and J. B. Kogut, Phys. Rev. Lett. **59**, 399 (1987).
[6] A. Bazavov *et al.* (HotQCD Collaboration), Phys. Lett. B **795**, 15 (2019).
[7] S. L. Adler, Phys. Rev. **177**, 2426 (1969).
[8] J. S. Bell and R. Jackiw, Nuovo Cimento A **60**, 47 (1969).
[9] S. L. Adler and W. A. Bardeen, Phys. Rev. **182**, 1517 (1969).
[10] D. J. Gross, R. D. Pisarski, and L. G. Yaffe, Rev. Mod. Phys. **53**, 43 (1981).
[11] R. D. Pisarski and F. Wilczek, Phys. Rev. D **29**, 338 (1984).
[12] M. Cheng *et al.*, Eur. Phys. J. C **71**, 1564 (2011).
[13] H. Ohno, U. M. Heller, F. Karsch, and S. Mukherjee, Proc. Sci., LATTICE2012 (**2012**) 095 [arXiv:1211.2591].
[14] V. Dick, F. Karsch, E. Laermann, S. Mukherjee, and S. Sharma, Phys. Rev. D **91**, 094504 (2015).
[15] H. T. Ding *et al.*, Phys. Rev. Lett. **123**, 062002 (2019).
[16] E. V. Shuryak, Comments Nucl. Part. Phys. **21**, 235 (1994).

[17] M. C. Birse, T. D. Cohen, and J. A. McGovern, Phys. Lett. B **388**, 137 (1996).
[18] S. H. Lee and T. Hatsuda, Phys. Rev. D **54**, R1871 (1996).
[19] N. J. Evans, S. D. H. Hsu, and M. Schwetz, Phys. Lett. B **375**, 262 (1996).
[20] M. I. Buchoff *et al.*, Phys. Rev. D **89**, 054514 (2014).
[21] A. Bazavov *et al.* (HotQCD Collaboration), Phys. Rev. D **86**, 094503 (2012).
[22] K. Suzuki, S. Aoki, Y. Aoki, G. Cossu, H. Fukaya, and S. Hashimoto (JLQCD Collaboration), Proc. Sci., LATTICE2018 (**2018**) 152 [arXiv:1812.06621].
[23] A. Tomiya, G. Cossu, S. Aoki, H. Fukaya, S. Hashimoto, T. Kaneko, and J. Noaki, Phys. Rev. D **96**, 034509 (2017); **96**, 079902(A) (2017).
[24] T.-W. Chiu, W.-P. Chen, Y.-C. Chen, H.-Y. Chou, and T.-H. Hsieh (TWQCD Collaboration), Proc. Sci., LATTICE2013 (**2014**) 165 [arXiv:1311.6220].
[25] S. Sharma, V. Dick, F. Karsch, E. Laermann, and S. Mukherjee, Nucl. Phys. **A956**, 793 (2016).
[26] B. B. Brandt, A. Francis, H. B. Meyer, O. Philipsen, D. Robaina, and H. Wittig, J. High Energy Phys. 12 (2016) 158.
[27] F. Karsch, E. Laermann, S. Mukherjee, and P. Petreczky, Phys. Rev. D **85**, 114501 (2012).
[28] A. Bazavov, F. Karsch, Y. Maezawa, S. Mukherjee, and P. Petreczky, Phys. Rev. D **91**, 054503 (2015).
[29] T. Hashimoto, A. Nakamura, and I. O. Stamatescu, Nucl. Phys. **B400**, 267 (1993).
[30] M. F. L. Golterman, Nucl. Phys. **B273**, 663 (1986).
[31] G. W. Kilcup and S. R. Sharpe, Nucl. Phys. **B283**, 493 (1987).
[32] R. Altmeyer, K. D. Born, M. Gockeler, R. Horsley, E. Laermann, and G. Schierholz (MT(c)), Nucl. Phys. **B389**, 445 (1993).
[33] S. Gupta, Phys. Rev. D **60**, 094505 (1999).
[34] G. P. Lepage, Phys. Rev. D **59**, 074502 (1999).
[35] E. Follana, Q. Mason, C. Davies, K. Hornbostel, G. P. Lepage, J. Shigemitsu, H. Trottier, and K. Wong (HPQCD and UKQCD Collaboration), Phys. Rev. D **75**, 054502 (2007).
[36] A. Bazavov *et al.* (MILC Collaboration), Proc. Sci., LATTICE2008 (**2008**) 033 [arXiv:0903.0874].
[37] A. Bazavov *et al.* (MILC Collaboration), Phys. Rev. D **82**, 074501 (2010).
[38] A. Bazavov and P. Petreczky (HotQCD Collaboration), Proc. Sci., LATTICE2010 (**2010**) 169 [arXiv:1012.1257].
[39] E. Follana, C. T. H. Davies, G. P. Lepage, and J. Shigemitsu (HPQCD and UKQCD Collaboration), Phys. Rev. Lett. **100**, 062002 (2008).
[40] A. Bazavov *et al.*, Phys. Rev. D **85**, 054503 (2012).
[41] A. Bazavov *et al.* (HotQCD Collaboration), Phys. Rev. D **90**, 094503 (2014).
[42] A. Bazavov *et al.*, Phys. Rev. D **95**, 054504 (2017).
[43] A. Bazavov, N. Brambilla, H. T. Ding, P. Petreczky, H. P. Schadler, A. Vairo, and J. H. Weber, Phys. Rev. D **93**, 114502 (2016).
[44] A. Bazavov, N. Brambilla, P. Petreczky, A. Vairo, and J. H. Weber (TUMQCD Collaboration), Phys. Rev. D **98**, 054511 (2018).
[45] P. Hegde, Proc. Sci., LATTICE2011 (**2011**) 014 [arXiv:1112.0364].
[46] H. Sandmeyer, Ph.D. thesis, Universität Bielefeld, 2019, https://doi.org/10.4119/unibi/2936264.
[47] H. Akaike, IEEE Trans. Autom. Control **19**, 716 (1974).
[48] J. E. Cavanaugh, Stat. Probab. Lett. **33**, 201 (1997).
[49] C. W. Bernard, M. C. Ogilvie, T. A. DeGrand, C. E. DeTar, S. A. Gottlieb, A. Krasnitz, R. L. Sugar, and D. Toussaint, Phys. Rev. Lett. **68**, 2125 (1992).
[50] C. W. Bernard, T. Blum, T. A. DeGrand, C. E. Detar, S. A. Gottlieb, A. Krasnitz, R. L. Sugar, and D. Toussaint, Phys. Rev. D **48**, 4419 (1993).
[51] C. W. Bernard, T. Burch, K. Orginos, D. Toussaint, T. A. DeGrand, C. E. Detar, S. Datta, S. A. Gottlieb, U. M. Heller, and R. Sugar, Phys. Rev. D **64**, 054506 (2001).
[52] M. Tanabashi *et al.* (Particle Data Group), Phys. Rev. D **98**, 030001 (2018).
[53] S. Prelovsek, Phys. Rev. D **73**, 014506 (2006).
[54] S. Prelovsek, C. Dawson, T. Izubuchi, K. Orginos, and A. Soni, Phys. Rev. D **70**, 094503 (2004).
[55] C. Bernard, C. E. DeTar, Z. Fu, and S. Prelovsek, Phys. Rev. D **76**, 094504 (2007).
[56] W.-J. Lee and S. R. Sharpe, Phys. Rev. D **60**, 114503 (1999).
[57] G. Aarts, C. Allton, D. de Boni, S. Hands, B. Jäger, C. Praki, and J.-I. Skullerud, EPJ Web Conf. **171**, 14005 (2018).
[58] S. Datta, S. Gupta, M. Padmanath, J. Maiti, and N. Mathur, J. High Energy Phys. 02 (2013) 145.
[59] S. Aoki, H. Fukaya, and Y. Taniguchi, Phys. Rev. D **86**, 114512 (2012).
[60] K. Suzuki, S. Aoki, Y. Aoki, G. Cossu, H. Fukaya, and S. Hashimoto (JLQCD Collaboration), EPJ Web Conf. **175**, 07025 (2018).
[61] C. E. Detar and J. B. Kogut, Phys. Rev. D **36**, 2828 (1987).
[62] K. D. Born, S. Gupta, A. Irback, F. Karsch, E. Laermann, B. Petersson, and H. Satz (MT(c)), Phys. Rev. Lett. **67**, 302 (1991).
[63] D. Banerjee, R. V. Gavai, and S. Gupta, Phys. Rev. D **83**, 074510 (2011).
[64] E. Laermann and F. Pucci, Eur. Phys. J. C **72**, 2200 (2012).
[65] S. Gupta and N. Karthik, Phys. Rev. D **87**, 094001 (2013).
[66] B. B. Brandt, A. Francis, M. Laine, and H. B. Meyer, J. High Energy Phys. 05 (2014) 117.
[67] M. Laine and M. Vepsalainen, J. High Energy Phys. 02 (2004) 004.
[68] M. Laine and Y. Schroder, J. High Energy Phys. 03 (2005) 067.
[69] E. Braaten and A. Nieto, Phys. Rev. D **53**, 3421 (1996).
[70] A. Bazavov, H. T. Ding, P. Hegde, F. Karsch, C. Miao, S. Mukherjee, P. Petreczky, C. Schmidt, and A. Velytsky, Phys. Rev. D **88**, 094021 (2013).
[71] H. T. Ding, S. Mukherjee, H. Ohno, P. Petreczky, and H. P. Schadler, Phys. Rev. D **92**, 074043 (2015).
[72] V. Koch, E. V. Shuryak, G. E. Brown, and A. D. Jackson, Phys. Rev. D **46**, 3169 (1992); **47**, 2157(E) (1993).
[73] E. V. Shuryak, Rev. Mod. Phys. **65**, 1 (1993).
[74] C. Rohrhofer, Y. Aoki, G. Cossu, H. Fukaya, C. Gattringer, L. Y. Glozman, S. Hashimoto, C. B. Lang, and S. Prelovsek, Phys. Rev. D **100**, 014502 (2019).